Optics Letters

Symmetry-preserving modeling for lithographic imaging

Shaopeng Guo,[1] Lei Cheng,[1] Hao Jiang,[1,2,5] Xianhua Ke,[3] Song Zhang,[1] David H. Wei,[3,6] Yanlong Sun,[4] and Shiyuan Liu[1,2,7]

[1]State Key Laboratory of Intelligent Manufacturing Equipment and Technology, Huazhong University of Science and Technology, Wuhan 430074, China
[2]Optics Valley Laboratory, Wuhan 430074, China
[3]Yuwei Optica Co., Ltd., Wuhan 430073, China
[4]Institute of Artificial Intelligence, Hefei Comprehensive National Science Center, Hefei 230088, China
[5]hjiang@hust.edu.cn
[6]david.hq.wei@gmail.com
[7]shyliu@hust.edu.cn

Received 24 April 2024; revised 4 June 2024; accepted 24 June 2024; posted 24 June 2024; published 15 July 2024

In computational imaging and lithography, it has been a challenge for a numerical model to faithfully preserve symmetries in the physical imaging system. In this Letter, we present a project-to-symmetry-subspace (PTSS) method to prevent symmetry loss during the iterative generation of optical kernels. Essentially, PTSS is to project iterative vectors onto a predefined symmetric subspace when decomposing the transmission cross coefficient (TCC). Simulation results demonstrate the PTSS-generation of a truncated set of optical kernels that are substantially free of symmetry error, regardless of the order of truncation.

https://doi.org/10.1364/OL.528120

In the field of model-based optical proximity correction (OPC), it is crucial to achieve accurate and efficient lithographic imaging modeling that adapts to continuously shrinking technology nodes [1–4]. Usually, lithography systems adopt symmetrical configurations in the semiconductor manufacturing process [5,6]. An accurate lithographic imaging simulation model should be able to faithfully reflect the physical symmetry inherent in the lithography system. For symmetric patterns in an integrated circuit (IC) layout, the aerial images from a lithographic imaging simulation should also be symmetric. This ensures that the resulting IC chip maintains operational characteristics in alignment with the design specifications. However, numerical processes such as quantization, sampling, error accumulation during iterations, especially irregular truncation of eigen vectors, often introduce asymmetry to the numerical model [7,8]. An asymmetric numerical model leads to a degraded simulation accuracy, thereby affecting the optimization outcomes and efficiency of OPC [7]. As feature sizes decrease, the impact of symmetry loss becomes more pronounced in OPC and other computational lithography (CL) applications. The sum of coherent systems (SOCS) is a widely used method for efficiently solving a photolithography aerial image model described by Hopkins' partially coherent imaging theory [9]. SOCS decomposes the four-dimensional transmission cross coefficient (TCC) matrix in the Hopkins' imaging formula into a sum of squares of convolutions, using eigenvalue decomposition (EVD) [10,11]. For a large matrix, iterative methods such as power iteration [12], Krylov subspace projection methods [13], Arnoldi iteration [14], Lanczos method [15,16] and their variants are widely employed for EVD. Given a symmetric TCC matrix, it is unfortunate that the existing EVD solvers do not guarantee that the generated eigen vectors, thus a truncated SOCS system, be symmetric. In [7], symmetry checking and enhancement procedures were proposed to ensure the generation of symmetric aerial images. However, it does not reduce the symmetry error in the TCC decomposition process. To the best of our knowledge, there is a lack of general guidelines on where to truncate the series to get the lowest symmetry error, and most of the issues have been addressed by trial-and-error selection and a combination of optical kernels obtained from the EVD solver. In this way, the algorithm needs to be frequently modified for different configurations of lithographic imaging systems and truncation orders of TCC decomposition, which can be a complex and time-consuming process. Hence, it is of great importance to enhance the symmetry preservation capability within the TCC decomposition.

In this Letter, we introduce a project-to-symmetry-subspace (PTSS) method to address the symmetry preservation issue in the lithographic imaging simulation. The aerial image $\mathbf{I}(\mathbf{r})$ generated by the projection exposure systems (steppers or scanners) can be characterized by the Hopkins' formulation of partially coherent imaging [17,18]

$$\mathbf{I}(\mathbf{r}) = \iint [\mathbf{M}(\mathbf{r}-\mathbf{r}_1)]^{+}\mathbf{TCC}(\mathbf{r}_1,\mathbf{r}_2)[\mathbf{M}(\mathbf{r}-\mathbf{r}_2)]\mathrm{d}\mathbf{r}_1\mathrm{d}\mathbf{r}_2, \quad (1)$$

where $\mathbf{r}$ is the two-dimensional (2D) image plane coordinates on the wafer, $\mathbf{r}_1$ and $\mathbf{r}_2$ are 2D object plane coordinates located on the mask, $\mathbf{M}(\cdot)$ represents the mask response function, the superscript + denotes the conjugate transpose operation of matrices,

and $\mathbf{TCC}(\mathbf{r}_1, \mathbf{r}_1)$ is the so-called TCC operator being defined as [19,20]

$$\mathbf{TCC}(\mathbf{r}_1, \mathbf{r}_2) = [\mathbf{P}(\mathbf{r}_1)]^{+}\mathbf{J}(\mathbf{r}_1, \mathbf{r}_2)\mathbf{P}(\mathbf{r}_2), \tag{2}$$

where $\mathbf{J}(\mathbf{r}_1, \mathbf{r}_2)$ is the mutual intensity function of the source and $\mathbf{P}(\cdot)$ is the point-spread function (PSF) of the projection system; both of them are represented in the frequency domain. The TCC operator contains all information about the lithographic imaging system except for the mask. As symmetrical illumination schemes and projection systems without odd-order aberrations are commonly employed, an imaging system is almost always symmetric with respect to the X- and Y-flip operations on the mask [6,19]. In this Letter, the idea of PTSS will be illustrated mostly using the X- and Y-flip symmetries although the same method and algorithm apply straightforwardly to other types of symmetry. By the SOCS method, the TCC operator is approximated by a Mercer expansion in terms of the eigenvalues $\{W_n\}_{n=1}^{N}$ and the corresponding optical kernels $\{\mathbf{K}_n(\mathbf{r})\}_{n=1}^{N}$ [21,22],

$$\mathbf{TCC}(\mathbf{r}_1, \mathbf{r}_2) \approx \sum_{n=1}^{N} w_n \mathbf{K}_n(\mathbf{r}_1)\mathbf{K}_n^{+}(\mathbf{r}_2), \tag{3}$$

where N is the truncation order for the approximate decomposition. For Hermitian operators, we use the Lanczos algorithm to implement the approximation process [16]. Let $\mathbf{q}_j$ denotes the orthonormal Lanczos vectors obtained from the Lanczos iterations, we can get optical kernels $\{\mathbf{K}_n(\mathbf{r})\}_{n=1}^{N}$ from the Krylov subspace $\mathbf{S}_N^q$ by similarity transformation [23],

$$\mathbf{S}_N^q = span\{\mathbf{q}_1, \mathbf{q}_2, \ldots, \mathbf{q}_N\}. \tag{4}$$

The TCC operator should faithfully reflect the symmetry of the actual lithographic imaging system, therefore naturally remains invariant under the parity operations P_x and P_y,

$$\begin{aligned} \mathbf{TCC} \cdot P_x[\mathbf{V}(x,y)] &= P_x[\mathbf{TCC} \cdot \mathbf{V}(x,y)], \\ \mathbf{TCC} \cdot P_y[\mathbf{V}(x,y)] &= P_y[\mathbf{TCC} \cdot \mathbf{V}(x,y)], \end{aligned} \tag{5}$$

where the operators P_x and P_y are defined, respectively, as the flip or mirror symmetry along the X and Y directions. For any vector $\mathbf{V}(x,y)$, we have

$$\begin{aligned} P_x[\mathbf{V}(x,y)] &\triangleq \mathbf{V}(-x,y), \\ P_y[\mathbf{V}(x,y)] &\triangleq \mathbf{V}(x,-y). \end{aligned} \tag{6}$$

Note that

$$P_x^2 = P_y^2 = \mathrm{I}, \tag{7}$$

$\mathbf{I}$ being the identity matrix, so P_x and P_y have eigenvalues λ_x, $\lambda_y = \pm 1$. It follows from Eq. (5) that TCC and P_x, P_y are simultaneously diagonalizable. A symmetry about X exists if $\mathbf{V}(x, y) = \mathbf{V}(-x, y)$ or an antisymmetry if $\mathbf{V}(x, y) = -\mathbf{V}(-x, y)$ holds for any vector $\mathbf{V}(x, y)$. The same is true for the Y direction. Accordingly, we use $\{\lambda_x, \lambda_y\}$ as symmetry signatures to group the optical kernels from the Lanczos solver into four sets. Symmetry signatures corresponding to the four sets are respectively,

$$\{(\lambda_x, \lambda_y)\} = \{(+1,+1), (-1,+1), (-1,-1), (+1,-1)\}. \tag{8}$$

Then, given any Lanczos vector $\mathbf{q}_j^{in}$, we make the following linear transformations before the next Lanczos iteration,

$$\begin{aligned} \mathbf{q}_j^{iny} &= (\mathbf{q}_j^{in} + \lambda_x \times P_x[\mathbf{q}_j^{in}])/2, \\ \mathbf{q}_j^{out} &= (\mathbf{q}_j^{iny} + \lambda_y \times P_y[\mathbf{q}_j^{iny}])/2. \end{aligned} \tag{9}$$

Four symmetric subspaces are formed by the sets of Lanczos vectors obtained after taking each pair of symmetry signatures

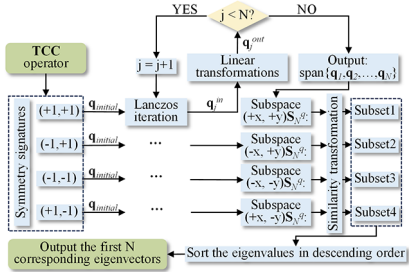

Fig. 1. Flowchart of TCC decomposition and projection processes.

from Eq. (8) and applying Eq. (9). Given the pair of symmetry signatures, $(\lambda_x, \lambda_y) = (+1, +1)$, the subspace $(+x, +y)\mathbf{S}_N^q$ can be constructed to characterize the components of the Lanczos vectors that are symmetric about both X and Y. Similarly, given $(\lambda_x, \lambda_y) = (-1, +1)$, the subspace $(-x, +y)\mathbf{S}_N^q$ is constructed to characterize the components that are anti-symmetric about X and symmetric about Y. Moreover, given $(\lambda_x, \lambda_y) = (-1, -1)$ and $(\lambda_x, \lambda_y) = (+1, -1)$, subspaces $(-x, -y)\mathbf{S}_N^q$ and $(+x, -y)\mathbf{S}_N^q$ respectively represent components that are anti-symmetric about both X and Y and symmetric about X and anti-symmetric about Y. Finally, we take Lanczos vectors from the four symmetric subspaces and use a similarity transformation to obtain the ultimate optical kernels $\{\mathbf{K}_n(\mathbf{r})\}_{n=1}^{N}$, which will maintain the same symmetry as the Lanczos vectors. This guarantees Eq. (5), as such the desired symmetry $\{\lambda_x, \lambda_y\}$ in the TCC operator, is preserved. In this way, for a layout pattern input that is symmetric about the X-flip and the Y-flip, we can obtain an aerial image intensity distribution that satisfies the same symmetry. This outlines the fundamental principle of the PTSS method, which has been disclosed in [24]. Figure 1 illustrates the flow of the TCC decomposition using the PTSS method. Substituting Eq. (3) into Eq. (1), we reformulate the aerial image equation as follows:

$$\begin{aligned} \mathbf{I}(\mathbf{r}) &= \sum_{n=1}^{N} w_n [\mathbf{M}^{+} \otimes \mathbf{K}_n](\mathbf{r}) \odot [\mathbf{K}_n^{+} \otimes \mathbf{M}](\mathbf{r}) \\ &= \sum_{n=1}^{N} w_n |[\mathbf{K}_n^{+} \otimes \mathbf{M}](\mathbf{r})|^2, \end{aligned} \tag{10}$$

where $\otimes$ represents the convolution operation between two functions or images, and $\odot$ denotes the Hadamard product.

To numerically validate the proposed PTSS method, we simulated a partially coherent lithographic imaging system described by Eq. (1). The light source is an annular illumination with inner and outer partial coherence factors of $\sigma_{\mathrm{in}} = 0.73$ and $\sigma_{\mathrm{out}} = 0.36$, respectively. The illumination wavelength is 193 nm, and the polarization state was set as unpolarized. The numerical aperture of the projection system is NA = 1.35, and the projection system is configured to be free of aberrations. When the optical model has odd aberrations, the required TCC symmetry is broken, and the PTSS method is no longer applicable. Equation (3) is implemented with the standard Lanczos method and the proposed PTSS. Figure 2(a) shows optical kernels obtained from the conventional Lanczos method. It is obvious that the symmetry is not preserved in these optical kernels. Figure 2(b) shows the optical kernels generated via the PTSS, which preserve symmetries and antisymmetries of the corresponding subspaces and represent optical point-spread responses with a definitive even or odd parity.

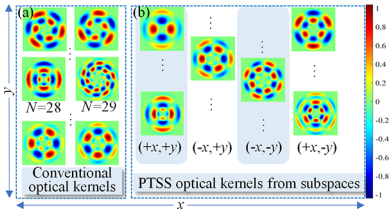

Fig. 2. Optical kernels obtained from (a) conventional Lanczos method and (b) PTSS.

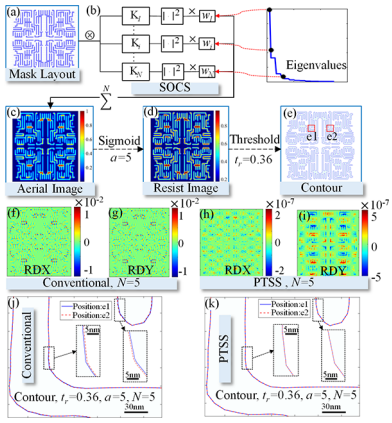

Fig. 3. (a) Designed mask pattern layout. (b) Imaging procedure corresponds to Eq. (10). (c) Normalized aerial image obtained from the conventional method with a truncation order of $N = 5$. (d) Resist image. (e) Contours extracted from the resist image based on a predetermined threshold. Relative differences between the aerial image obtained from the conventional method and its flipped images along (f) X and (g) Y. Relative differences between the aerial image obtained from the PTSS and its flipped images along (h) X and (i) Y. Comparison result of contours obtained from (j) conventional method and (k) PTSS at symmetric positions e1 and e2 in (e).

Then, we designed a target mask layout with a pattern that exhibits symmetry under X- and Y-flips, as seen in Fig. 3(a). The critical dimension (CD) of the target layout is 45 nm. We utilized an in-house rasterization algorithm to implement the process of polygon-to-image and obtain the pixelated mask response function $\mathbf{M}(\cdot)$ in Eqs. (1) and (10). It is important to ensure that $\mathbf{M}(\cdot)$ depends only on spatial coordinates and preserves the X- and Y-flip symmetries. The procedure of calculating the aerial image using the optical kernels and mask response function, as described by Eq. (10), is illustrated graphically in Fig. 3(b). Figure 3(c) shows the normalized aerial image $\mathbf{I}(x, y)$ obtained from Fig. 3(b), and the corresponding optical kernels was calculated by the conventional Lanczos method with a truncation order of $N = 5$. The resist effect can be modeled with a sigmoid function [25],

$$\mathbf{I}^{\text{resist}} = \text{sigmoid}(\mathbf{I}^{\text{aerial}}, a, t_r) = \frac{1}{1 + \exp[-a(\mathbf{I}^{\text{aerial}} - t_r)]}, \quad (11)$$

where a is the steepness index of the sigmoid function, and t_r is the threshold of resist. It is reasonable to deduce that the sigmoid function has no effect on the aerial image's symmetry. Figure 3(e) shows the contours extracted from the resist image in Fig. 3(d) based on a predetermined threshold $t_r = 0.36$, and $a = 5$. Relative differences between the aerial image $\mathbf{I}(x, y)$ and its flipped images $P_x[\mathbf{I}(x, y)]$, $P_y[\mathbf{I}(x, y)]$ can be calculated by

$$RDX = [\mathbf{I}(x, y) - P_x[\mathbf{I}(x, y)]]/\max(\mathbf{I}(x, y)),$$
$$RDY = [\mathbf{I}(x, y) - P_y[\mathbf{I}(x, y)]]/\max(\mathbf{I}(x, y)), \quad (12)$$

where $\max(\mathbf{I}(x, y))$ denotes the maximum value in the aerial image matrix $\mathbf{I}(x, y)$. In addition to indicating the symmetry error of aerial images in the X and Y directions, the values of *RDX* and *RDY* indirectly reflect symmetry errors of the TCC operator. The results of the conventional method's *RDX* and *RDY* are displayed in Figs. 3(f) and 3(g), respectively, showing symmetry errors in the order of 10^{-3} to 10^{-2}. However, with the application of the PTSS, the symmetry errors in both directions are significantly reduced to the order of 10^{-7}, as illustrated in Figs. 3(h) and 3(i). In Figs. 3(h), 3(i), and 3(k), $N = 5$ denotes the total number of (symmetric) kernels, in the same manner as in Figs. 3(f), 3(g), and 3(j). The symmetries of the first five symmetric kernels are (+x, +y), (+x, +y), (+x, −y), (−x, +y), and (−x, +y). Figure 3(j) depicts the comparison of contours obtained from the conventional method at symmetric positions e1 and e2 in Fig. 3(e). The difference in contours at positions e1 and e2 indicates that a symmetric pattern results in asymmetric contours after simulation. Figure 3(k) depicts the comparison of contours obtained from the PTSS at symmetric positions e1 and e2 in Fig. 3(e). As expected, the contours of the symmetric pattern remain symmetric, indicating that the PTSS effectively preserves the symmetry of the imaging system.

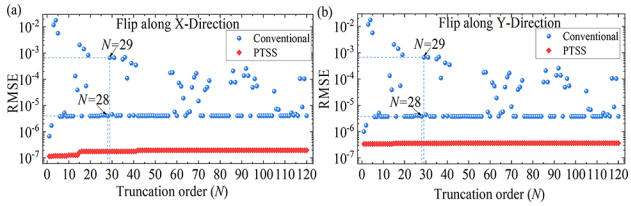

Fig. 4. As the truncation order ranges from 1 to 120, the *RMSE* variation for both methods with (a) X-flipped and (b) Y-flipped.

Furthermore, we investigated the variation of the symmetry errors in simulated aerial images at different truncation orders. To measure these errors, we calculate the overall difference between the simulated aerial image, and it is flipped image using the root mean square error (RMSE),

$$RMSE = \sqrt{\frac{1}{m}\sum_{j=1}^{m}[\mathbf{I}(x, y) - P[\mathbf{I}(x, y)]]^2}, \quad (13)$$

where P can be P_x or P_y, m denotes the total number of elements in the aerial image matrix $\mathbf{I}(x, y)$. Fig. 4(a) shows the *RMSE* variation for both methods with X-flipped when the truncation order varies from 1 to 120. For the conventional method, the *RMSE* typically falls within the range of 10^{-3} to 10^{-6} and varies across several orders of magnitude as the optical kernels used in the imaging process change once. Consider the case where the truncation order is 28, resulting in an *RMSE* at the level of 10^{-6}. However, upon adding one more kernel, the *RMSE* increases to the level of 10^{-4}. It suggests that the 29th kernel contributes to a significant amount of symmetry error, as the conventional method produces an asymmetric kernel that looks like the one depicted in Fig. 2(a). Since the conventional method cannot guarantee symmetrical optical kernels, it requires several optical kernels near the truncation order be kept and grouped

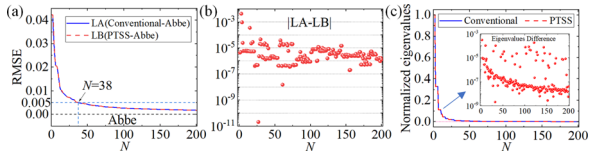

Fig. 5. (a) Comparison of model errors among the PTSS TCC, the conventional TCC, and the Abbe methods. Comparison of (b) accuracy and (c) eigenvalues for the two TCC methods.

together to cancel their asymmetries. But it is highly non-trivial to decide which kernels should be grouped and kept. By contrast, our PTSS method effectively avoids the symmetry loss caused by the truncation, maintaining a near-zero *RMSE* at the level of 10^{-7}. As a result, the number of optical kernels can be freely chosen as needed without a delicate kernel selection process. As shown in Fig. 4(b), the *RMSE* variations for both methods exhibit a similar trend for the Y-flip. Other factors, such as quantization, sampling, and error accumulation during iterations, can also contribute to the *RMSE*. Nevertheless, the PTSS approach consistently outperforms the conventional method with an *RMSE* that is always an order of magnitude below.

In Fig. 5(a), an aerial image by the Abbe method [26] is taken as the ground truth. The differences between the ground truth and the results of the conventional and PTSS methods are measured in *RMSE*. The model errors for both TCC methods decrease almost synchronously as the number of kernels increases. With an *RMSE* of 0.005 set as a permissible limit, at least 38 kernels are needed for accurate imaging. Figure 5(b) shows the *RMSE* differences between the two TCC methods, while Fig. 5(c) illustrates the variations and differences in eigenvalues between them.

In conclusion, we have demonstrated a PTSS method that ensures the generation of symmetric kernels during TCC decomposition, where the iterative vectors are repeatedly projected onto predefined symmetric subspaces. The effectiveness of PTSS has been verified by simulating the aerial image and contour of a symmetric pattern under a symmetric TCC. Unlike the conventional methods that suffer from EVD-induced asymmetries, the PTSS method always generates a fully symmetric model, regardless to which order the TCC eigenvectors are truncated.

Funding. National Natural Science Foundation of China (52130504, 52205592); Key Research and Development Plan of Hubei Province (2022BAA013); Major Program (JD) of Hubei Province (2023BAA002); Innovation Project of Optics Valley Laboratory (OVL2023PY003).

Acknowledgment. The authors would like to express their thanks to the technical support from the Experiment Centre for Advanced Manufacturing and Technology in School of Mechanical Science and Engineering of HUST.

Disclosures. The authors declare the following: Xianhua Ke and David H. Wei have financial interests in Yuwei Optica Co., Ltd., a company focusing on computational lithography and holding patents related to technologies for lithography modeling and applications.

Data availability. Data underlying the results presented in this paper are not publicly available at this time but may be obtained from the authors upon reasonable request.

REFERENCES

1. A. Erdmann, T. Fühner, P. Evanschitzky, *et al.*, Microelectron. Eng. **132**, 21 (2015).
2. X. Ma, S. Zhang, Y. Pan, *et al.*, Laser Optoelectron. Prog. **59**, 0922008 (2022).
3. G. Chen, S. Li, and X. Wang, Opt. Express **29**, 17440 (2021).
4. Y. Shen, Opt. Express **25**, 21775 (2017).
5. B. Yenikaya, Proc. SPIE **10147**, 146 (2017).
6. P. Yu, W. Qiu, and D. Z. Pan, IEEE Trans. Semicond. Manufact. **21**, 638 (2008).
7. J. Lei, M. Sanie, and D. K. Lay, Proc. SPIE **4692**, 465 (2002).
8. C. Zuniga and E. Tejnil, Proc. SPIE **6520**, 65203I (2007).
9. N. B. Cobb, "Fast optical and process proximity correction algorithms for integrated circuit manufacturing," Ph.D. dissertation (University of California, 1998).
10. P. Gong, S. Liu, W. Lv, *et al.*, J. Vac. Sci. Technol. B **30**, 06FG03 (2012).
11. R. Sabatier, C. Fossati, S. Bourennane, *et al.*, Opt. Express **16**, 15249 (2008).
12. G. H. Golub and C. F. Van Loan, *Matrix Computations*, 4th ed. (JHU Press, 2013), Chap. 8.
13. Y. Saad, *Numerical Methods for Large Eigenvalue Problems*, 2nd ed. (SIAM, 2011), Chap. 6.
14. W. E. Arnoldi, Q. Appl. Math. **9**, 17 (1951).
15. C. Lanczos, J. Res. Natl. Bur. Stan. **45**, 255 (1950).
16. Y. Saad, *Iterative Methods for Sparse Linear Systems*, 2nd ed. (SIAM, 2003), Chap. 6.
17. H. H. Hopkins, Proc. R. Soc. Lond. A **217**, 408 (1953).
18. A. K.-K. Wong, *Optical Imaging in Projection Microlithography* (SPIE Press, 2005), Chap. 4.
19. X. Wu, S. Liu, W. Liu, *et al.*, Proc. SPIE **7544**, 75440Z (2010).
20. S. Liu, X. Zhou, W. Lv, *et al.*, Opt. Lett. **38**, 2168 (2013).
21. K. Yamazoe, J. Opt. Soc. Am. A **25**, 3111 (2008).
22. K. Yamazoe, J. Opt. Soc. Am. A **29**, 2591 (2012).
23. L. Komzsik, *The Lanczos Method: Evolution and Application* (SIAM, 2003), Chap. 1.
24. H. Wei and X. Ke, "Optical imaging method, device and system for photolithography system," U.S. patent 2024 0126179 A1 (18 April 2024).
25. S. Zhang, X. Ma, and J. Zhang, Opt. Express **31**, 36451 (2023).
26. X. Ma, Y. Li, and L. Dong, J. Opt. Soc. Am. A **29**, 1300 (2012).